OUKA
The University of Osaka
Institutional Knowledge Archive

Title	Controlled Activation of Reactive Oxygen Species by Atomic Force Microscopy: Synthesis of Superoxo and Ozone Molecules on Rutile TiO2 (110) Surface
Author(s)	Adachi, Yuuki; Wen, Huan Fei; Sugawara, Yasuhiro et al.
Citation	ChemCatChem. 2025, 17(24), p. e01138
Version Type	VoR
URL	https://hdl.handle.net/11094/103588
rights	This article is licensed under a Creative Commons Attribution-NonCommercial-NoDerivatives 4.0 International License.
Note	

The University of Osaka Institutional Knowledge Archive : OUKA

https://ir.library.osaka-u.ac.jp/

The University of Osaka

Check for updates

ChemCatChem

Research Article
doi.org/10.1002/cctc.202501138

Chemistry Europe
European Chemical Societies Publishing

www.chemcatchem.org

Controlled Activation of Reactive Oxygen Species by Atomic Force Microscopy: Synthesis of Superoxo and Ozone Molecules on Rutile TiO_2 (110) Surface

Yuuki Adachi,[a] Huan Fei Wen,[a, b] Yasuhiro Sugawara,[a] Martin Konôpka,[c] Ján Brndiar,[d] Ivan Štich,[d] and Yan Jun Li*[a]

Electron-hole activation, transforming closed- to open-shell reactive oxygen species on photocatalytic TiO_2 surfaces, is essential for designing effective photocatalysts capable of providing specific functionalities and enhanced performance. However, at atomic level, the activation mechanism of the oxygen species remains murky. To shed light, we used a combination of atomic force microscopy, Kelvin probe force spectroscopy under ultra-high vacuum conditions with density functional theory simulations to understand the atomic-scale mechanism of electron and hole injection into the chemisorbed oxygen species supported on the rutile TiO_2 (110) surface. Specifically, the closed-shell oxygen species, such as the peroxo (O_2^{2-}) molecule , can be manipulated by applied local electric field to induce its hopping between different adsorption sites or molecular rotation, while the open-shell oxygen species, such as the superoxo (O_2^-) molecule, can be synthesized by injecting holes into their corresponding closed-shell form. Combining applied local electric field with hole injection we have been able to activate a tip-induced Langmuir–Hinshelwood reaction leading to ozone (O_3) molecule formation and, for the first time, visualize its synthesis at atomic resolution. The formation of long-lived superoxo and ozone molecules directly demonstrates their strong oxidative properties, which persist on the timescale of seconds highlighting their prominent role in photocatalysis.

1. Introduction

TiO_2 surfaces have received considerable attention from both fundamental and technological perspectives, largely due to their wide-ranging applications in photocatalysis, including organic pollutant decomposition, carbon monoxide oxidation, and water splitting.[1–4] The photogenerated electron-hole pairs can activate redox chemistry, for example by reaction with H_2O and O_2 molecules, leading to formation of reactive oxygen species (ROS), such as —OH, H_2O_2, O_2^-, or $^1O_2$. The ROS can then initiate various kinds of photocatalytic reactions.[5–8] Over the past decades, TiO_2(110) surfaces have been extensively studied, both experimentally and theoretically. Defects and surface reconstructions[9–13] have been shown to play a particularly important role on rutile TiO_2 surfaces by forming centers of excess charge, polarons, which then may act as active sites for anchoring atoms and molecules.[10,11] In addition to photogenerated electron-hole pairs, polarons may serve as an additional electron source for redox state chemistry, thereby enhancing their oxidation potential and enabling various challenging chemical transformations on TiO_2 surfaces.

ROS represent the most important on-surface species on TiO_2 surfaces. ROS are produced by activating H_2O or O_2 molecules adsorbed on TiO_2 surfaces by electrons or holes which are subsequently stabilized in various charge states and adsorption structures.[14–27] Once formed, ROS on TiO_2 surfaces readily react with various molecules, including water and hydrogen.[22–25] ROS also serve as key intermediates and precursors to hydroxyl radicals.[8] In recent years, reaction products derived from these processes have been observed at atomic resolution mostly using scanning tunneling microscopy (STM).[18–27] However, using STM, directly identifying both the adsorption structure and charge state of ROS is difficult. The difficulty arises for two reasons. First, the STM imaging mechanism reflects not only the adsorption structure but also the local density of states. Second, because STM relies on tunneling currents, during measurements electrons or holes are inevitably injected into the on-surface species thus potentially altering the adsorption structure or

[a] Y. Adachi, H. F. Wen, Y. Sugawara, Y. J. Li
Department of Applied Physics, Osaka University, 2-1 Yamadaoka, Suita, Osaka 565-0871, Japan
E-mail: liyanjun@ap.eng.osaka-u.ac.jp

[b] H. F. Wen
Key Laboratory of Instrumentation Science and Dynamic Measurement, School of Instrument and Electronics, North University of China, Taiyuan, Shanxi 030051, China

[c] M. Konôpka
Faculty of Electrical Engineering and Information Technology, Institute of Nuclear and Physical Engineering, Slovak University of Technology in Bratislava, Bratislava 841 04, Slovakia

[d] J. Brndiar, I. Štich
Institute of Informatics, Slovak Academy of Sciences, Bratislava 845 07, Slovakia

Supporting information for this article is available on the WWW under https://doi.org/10.1002/cctc.202501138

© 2025 The Author(s). ChemCatChem published by Wiley-VCH GmbH. This is an open access article under the terms of the Creative Commons Attribution-NonCommercial-NoDerivs License, which permits use and distribution in any medium, provided the original work is properly cited, the use is non-commercial and no modifications or adaptations are made.

© 2025 The Author(s). ChemCatChem published by Wiley-VCH GmbH

charge state of the ROS.[26,27] Consequently, identifying both the adsorption structure and the charge state of ROS using STM remains extremely challenging. To overcome this limitations, atomic force microscopy (AFM) has recently been employed to identify adsorption structures and charge states of ROS[15–17,28–33] on TiO_2 surfaces. The main advantage of AFM is that by operating at zero bias voltage, it enables direct visualization of adsorbate structures without unwanted electron/hole injection during scanning. By contrast, combination of AFM with Kelvin probe force spectroscopy (KPFS) makes a precise control of the charge states of ROS possible. In KPFS, a charge state modification is signaled by distinct jumps in the frequency shift (Δf) as a function of the applied voltage.[34–36] KPFS emulates what is done in photocatalysis where the photoexcited electron–hole pairs modify the redox chemistry of the ROS supported on the TiO_2 surface. In the KPFS experiment the redox chemistry is controlled by sample bias by injection of single electrons or holes from the tip in a controlled way to one predetermined ROS species, i.e., with atomic resolution.[34–37] It has been demonstrated experimentally that tip-generated species via redox-state manipulation are identical to those synthesized by transferring photo-generated electrons following irradiation of the sample with UV light.[31] However, to date AFM/KPFS studies have been limited to adatom species (O^0_{ad}, O^-_{ad}, O^{2-}_{ad}) and to molecular oxygen peroxo species (O_2^{2-}), leaving the other types of ROS largely unexplored.[11,12,28,29] In particular, activating adsorption of the superoxo (O_2^-) or ozone (O_3) ROS[7] have not yet been thoroughly investigated experimentally.[31,38]

In this study we investigate molecular ROS adsorbed on rutile TiO_2 (110) surface[14] at 78 K under ultrahigh vacuum (UHV) conditions. Although differences in photocatalytic activity of the major TiO_2 polymorphs, rutile and anatase, are still under debate,[5–8] we have opted to study the adsorption on the former. We focus on activation of O_2^{2-} by inducing jumps of the peroxo molecule between different adsorption sites or molecular rotation. We tip synthetize on-surface superoxo O_2^- molecule and determine its stable adsorption state and lifetime. Especially, formation of O_2^- from O_2^{2-} is considered one of the most important processes, as O_2^- is an open-shell species, in contrast to the closed-shell O_2^{2-}, and is therefore believed to exhibit much higher reactivity.[7] Despite its significance, only a few studies have provided experimental evidence for the formation of O_2^- from O_2^{2-} on TiO_2 surfaces, and they rely on indirect assembly methods.[7,8,39] Consequently, the formation mechanism of O_2^- on rutile TiO_2 remains largely unexplored at atomic resolution. Increasing attention has recently also been directed toward the utilization of ozone on TiO_2 surfaces. Since O_3 is highly toxic, its formation and decomposition must be carefully controlled to avoid health and environmental risks.[5,40–42] Hence, formation and decomposition of O_3 on TiO_2 have been investigated to assess their feasibility. For example, O_3 has recently been shown to decompose on illuminated TiO_2 surfaces under relative humidity, whereas its formation is observed when TiO_2 surfaces are exposed to NO^x under illumination.[5,40,41,42] However, these methods are macroscopic and unable to resolve microscopic details. Thus, the atomic-scale mechanism of O_3 formation on TiO_2 surfaces still remains a challenge.

To this end, we first demonstrate control over the adsorption structure of the closed-shell oxygen species, with a focus on the O_2^{2-} peroxo molecule on the rutile TiO_2 surface. We then synthesize the open-shell O_2^- superoxo molecule by injecting a hole into the corresponding closed-shell species. Finally, we synthesize the on-surface ozone molecule (O_3), which, based on density functional theory (DFT) modeling, we assign to be doubly charged (O_3^{2-}). To avoid unintended charge transfer during ROS imaging, we employ AFM at zero bias. The adsorption structure and charge state of ROS are controlled by KPFS. The molecular ROS studied here, O_2^- and O_3^{2-}, exhibit remarkable stability, with the former showing lifetimes on the order of seconds and the latter persisting for hundreds of seconds. Although there are other numerous AFM studies of various oxygen species on both rutile[15–17,29,31] and anatase[32] TiO_2 surfaces, to the best of our knowledge, our study is the first experimental AFM study where the O_3 molecular ROS could be prepared on a TiO_2 surface by tip induced redox state reaction. Superoxo O_2^- molecule could be prepared by tip charging of a neutral O_2 molecule on the anatase polymorph where it also forms naturally upon O_2 adsorption[32] but no redox state manipulation formation of the superoxo molecule on the rutile polymorph was reported.

2. Results and Discussion

2.1. Oxygen Species on Rutile TiO_2 (110) Surface

Large-scale image of the various oxygen species on the rutile TiO_2 (110) surface is shown in Figure 1a. The image shows with atomic resolution the rutile TiO_2 (110) surface after exposure to oxygen at room temperature. In Figure 1a, several bright spots can be observed on top of the dark Ti_{5c} rows, see panel b for atom labeling. In practice, a sample preparation in UHV leads to creation of point defects that produce excess electrons which are localized as polarons and provide a natural source of electronic charge for adsorbents, such as the electronegative oxygen atoms and molecules.[10,11] The charge states of oxygen adatoms have been studied previously.[15,16,29,30] Singly/doubly charged oxygen adatoms (O^-_{ad}/O^{2-}_{ad}) appear as small /large bright spots, respectively, which can form pairs of adatoms with various charges, $O^-_{ad}-O^-_{ad}$, $O^{2-}_{ad}-O^{2-}_{ad}$, $O^{2-}_{ad}-O^-_{ad}$, see Figure 1a.[15,16,29,30] We note that, since O^-_{ad} has an unfilled p-orbital, it is as an open-shell species, whereas O^{2-}_{ad}, with its fully filled p-orbital, is a closed-shell species.

In Figure 1a, we also find two types of peroxo molecule, O_2^{2-}(I) and O_2^{2-}(B), which differ by their adsorption geometry, i.e., doubly charged molecule adsorbed on-top of a Ti_{5c} atom and in the bridge position, see Figure 1b and Figure 2 for structural models. In line with the brightness difference between O_2^{2-}(I) and O_2^{2-}(B), the line profiles in panel **c** suggest that the height of O_2^{2-}(I) is indeed larger than that of O_2^{2-}(B), for more experimental details, see Figure S1. The most salient differences between O_2^{2-}(I) and O_2^{2-}(B) is that the molecular axis of the former is inclined by $\approx 45°$ with respect to the O- and Ti-rows, whereas no such angular feature is found for the latter, a fingerprint making the

© 2025 The Author(s). ChemCatChem published by Wiley-VCH GmbH

18673899, 0, Downloaded from https://chemistry-europe.onlinelibrary.wiley.com/doi/10.1002/cctc.202501138 by The University Of Osaka, Wiley Online Library on [11/12/2025]. See the Terms and Conditions (https://onlinelibrary.wiley.com/terms-and-conditions) on Wiley Online Library for rules of use; OA articles are governed by the applicable Creative Commons License

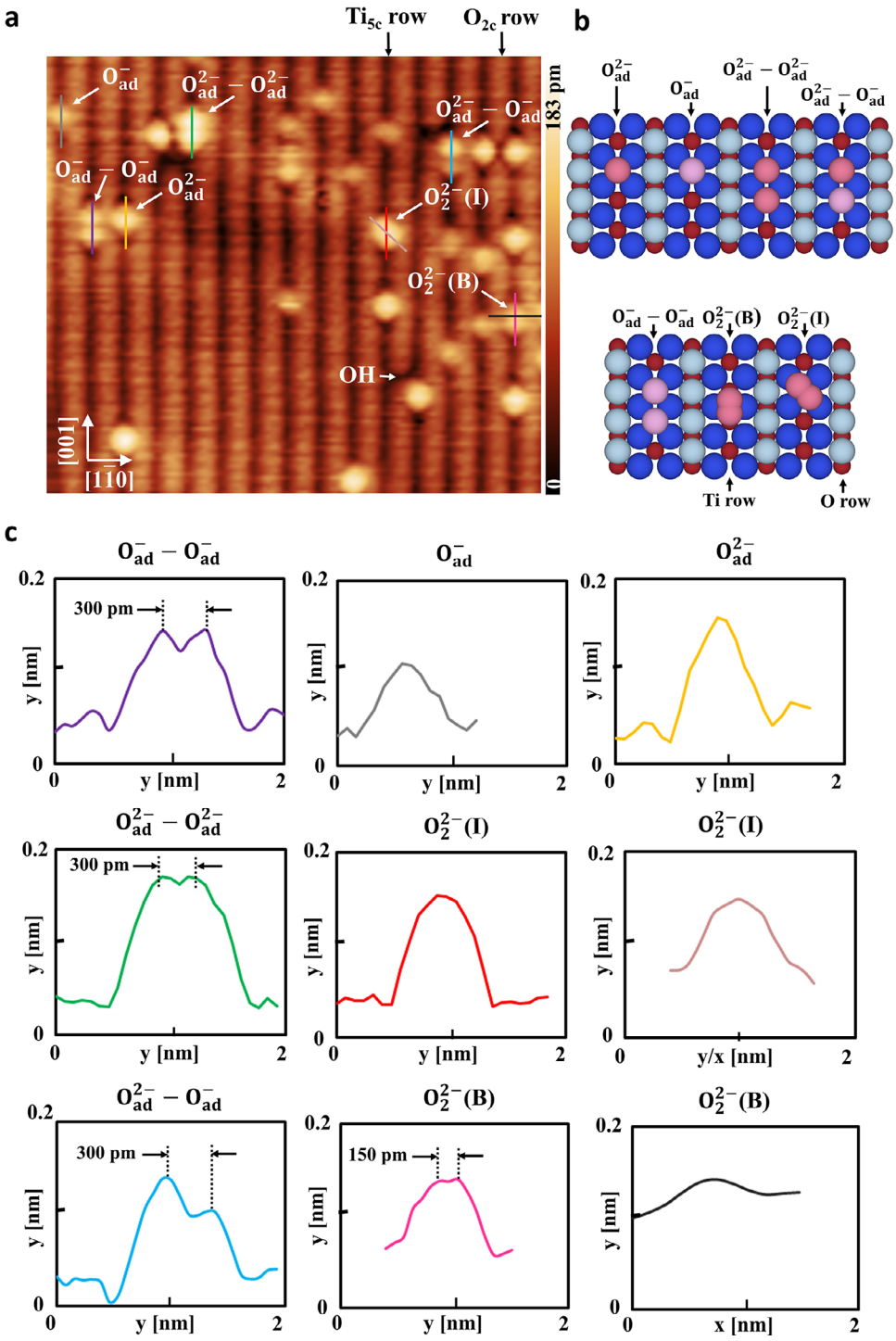

Figure 1. Large-scale image of various on-surface oxygen species adsorbed on rutile TiO_2 (110)-(1 × 1) surface. a) AFM image of rutile TiO_2 (110)-(1 × 1) surface after exposure to oxygen gas. Rows of O_{2c} and Ti_{5c} atoms on TiO_2 (110) are observed, using hole mode tip, as bright and dark areas, respectively. Negatively charged adatoms O^{2-}_{ad} , adatom pairs, O^{-}_{ad} . $O^{2-}_{ad} - O^{2-}_{ad}$, $O^{-}_{ad} - O^{-}_{ad}$, $O^{2-}_{ad} - O^{-}_{ad}$, and molecules O_2^{2-}(I), O_2^{2-} (B) are observed adsorbed on Ti_{5c} rows. Imaging parameters: constant Δf mode, $V_s = 0$ V. **b**) Structural models for the various on-surface oxygen species. O_{2c} (light blue balls): two-fold coordinated bridge oxygen row; O_{3c} (blue balls): in plane three-fold coordinated oxygen; Ti_{5c} (red balls): rows of five-fold coordinated Ti atoms; oxygen adatom (pink balls of various intensity reflecting their redox state). **c**) Line profiles measured on top of the oxygen species displayed with different colors corresponding to panel **a**.

© 2025 The Author(s). ChemCatChem published by Wiley-VCH GmbH

18673899, 0, Downloaded from https://chemistry-europe.onlinelibrary.wiley.com/doi/10.1002/cctc.202501138 by The University Of Osaka, Wiley Online Library on [11/12/2025]. See the Terms and Conditions (https://onlinelibrary.wiley.com/terms-and-conditions) on Wiley Online Library for rules of use; OA articles are governed by the applicable Creative Commons License

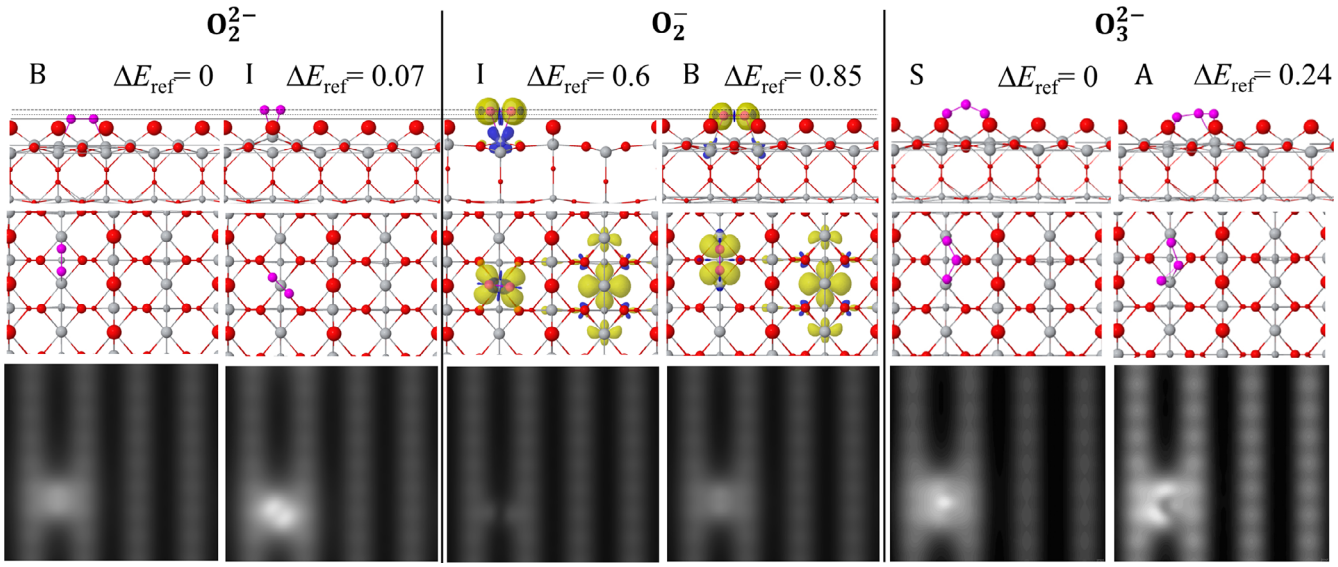

Figure 2. DFT simulations of oxygen molecules. From left to the right simulation results for O_2^{2-}(B), O_2^{2-}(I), O_2^-(I), O_2^-(B), O_3^{2-}(S), and O_3^{2-}(A). From top to the bottom adsorption energies (in eV), ball-and-stick structural models in side and top view, and simulated images calculated from local potentials, see the text and Supporting Information. The superimposed yellow/blue isosurfaces depict the up/down spin densities, respectively. Although no spin densities are seen for the singlet state peroxide O_2^{2-}, and O_3^{2-} molecules, the superoxo O_2^- molecule forms a doublet and, hence, forms a spin density around it. Note also the spin density of a polaron which forms from the H-defect built in our model, see the Supporting Information.

O_2^{2-}(I) relatively easy to identify. These conclusions are corroborated by DFT modeling, see Figure 2, which, in addition, suggest only a minor, <0.1 eV, energy differences between O_2^{2-}(I) and O_2^{2-}(B), while much larger, ≈0.6 eV, difference with respect to the superoxol, O_2^-, molecule, and thus explaining why the initial charge state of oxygen molecules is minus two: O_2^{2-}(I) and O_2^{2-}(B) in Figure 1a. This assignment agrees well with the previous results.[15] Finally, note that the distance between the two oxygen atoms in O_2^{2-}(B) is ≈ 150 pm, while the distance between the adatom pairs ($O_{ad}^- - O_{ad}^-$, $O_{ad}^{2-} - O_{ad}^{2-}$, $O_{ad}^{2-} - O_{ad}^-$) is ≈ 300 pm, see panel **c** in Figure 1, allowing us to safely distinguish the molecular O_2^{2-}(B) species from adatom pairs. Perhaps surprisingly, we find much richer distribution of O_{ad} species compared to the related AFM experiments in Ref. [31] where only doubly charged O_{ad}^{2-} atomic species were reported. We have found the same rich distribution of O_{ad} species also previously.[15,16,29] Such differences are most likely due to variations in sample preparation, which lead to different local distribution of the polarons and thus affect the oxygen adsorption.[9,14,21] Interestingly, deposition of O_2 molecules to the anatase TiO_2 surface, results in physisorbed neutral O_2 molecules and chemisorbed superoxo O_2^- molecules.[32]

The above experimental assignments are supported by DFT simulations of the oxygen molecular species, O_2^{2-}(B), O_2^{2-}(I), O_2^-(I), and O_2^-(B), shown in Figure 2, which also anticipates the results for the ozone molecule, O_3^{2-}, studied below. The simulations suggest that the energetical stability decreases in the order: O_2^{2-}(B), O_2^{2-}(I), O_2^-(I), and O_2^-(B). The simulated images allow a simple and unmistakable assignment of the O_2^{2-}(B) and O_2^{2-}(I) peroxide adsorption geometries simply by their different angular features and brightness. Note also that there is an angular signature of the O_2^-(I) species, akin to O_2^{2-}(I) (84° versus 45°). In Figure 2, the superimposed yellow/blue isosurfaces depict the up/down spin densities, respectively. Therefore, no spin densities are seen for the peroxide O_2^{2-} and ozone O_3^{2-} molecules in singlet state, the superoxo O_2^- molecule forms a doublet and, hence, forms a spin density around it. These results indicate that O_2^{2-} and O_3^{2-} are closed-shell species and O_2^- are open-shell species . The results of our DFT simulations are in fair agreement with those of Ref. [31]. More details on the adsorption geometries and electronic structure are in Figures S9-S16 in Supporting Information (SI).

2.2. Manipulation of Closed Shell Oxygen Species

2.2.1. O_2^{2-}(B) to O_2^{2-}(I) Manipulation

Now, we show that the closed shell oxygen molecule can be manipulated on the rutile TiO_2 surface, for full data set, see Figure S2. Figure 3a,b shows the AFM image of O_2^{2-}(B) consecutively manipulated to O_2^{2-}(I) by KPFS without desorption. The corresponding KPFS spectra are shown in Figure 3c. AFM images in Figure 3a,b are all taken at 0 V without tip-change, thus allowing a direct comparison of the topographic heights of the various oxygen species shown in Figure 3d,e. Figure 3a shows the initially adsorbed O_2^{2-}(B) oxygen molecule that symmetrically bridges two substrate Ti_{5c} atoms. After taking the image in Figure 3a, the tip was brought atop of O_2^{2-}(B) and the bias voltage was ramped from zero in the negative direction until a steep jump in Δf appeared, and then back to zero, as shown in Figure 3c. The AFM image of the same scan area taken at 0 V immediately thereafter, Figure 3b, shows that the initial image of the O_2^{2-} (B) species changed into an elliptical bright spot we associate with O_2^{2-}(I). This finding indicates that manipulation of the oxygen species occurred by the local electric field and implies that the O_2^{2-}(B) → O_2^{2-}(I) reorganization energy is smaller

© 2025 The Author(s). ChemCatChem published by Wiley-VCH GmbH

18673899, 0, Downloaded from https://chemistry-europe.onlinelibrary.wiley.com/doi/10.1002/cctc.202501138 by The University Of Osaka, Wiley Online Library on [11/12/2025]. See the Terms and Conditions (https://onlinelibrary.wiley.com/terms-and-conditions) on Wiley Online Library for rules of use; OA articles are governed by the applicable Creative Commons License

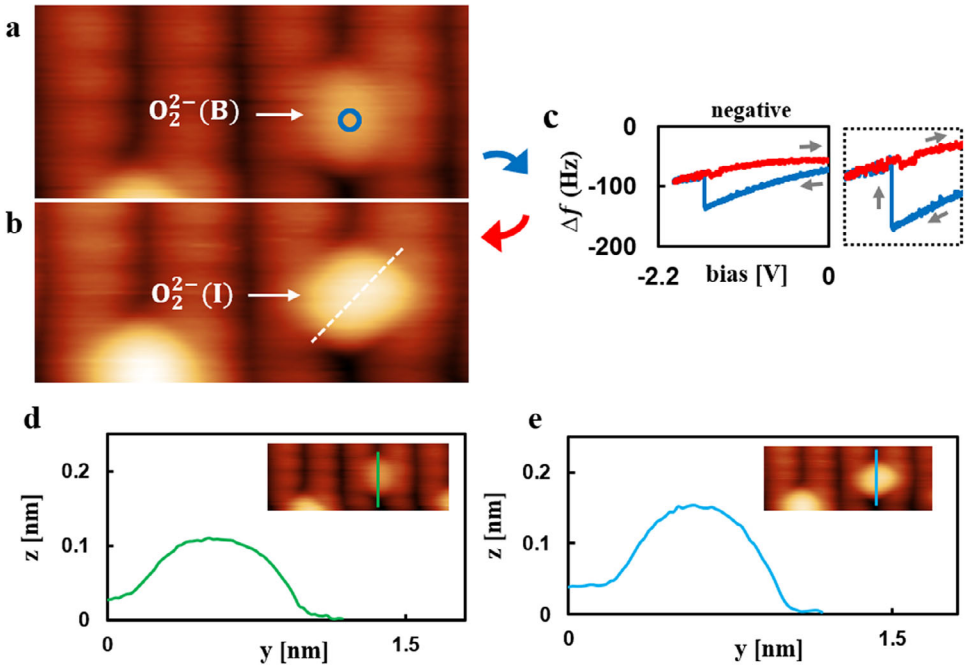

Figure 3. Closed shell oxygen molecule manipulation. a) AFM image of O_2^{2-}(B) adsorbed on the rutile TiO_2(110) surface. **b**) AFM image after KPFS manipulation of O_2^{2-}(B) with the tip positioned on top of the target oxygen species. Imaging parameters for **a, b**; constant Δ^f mode, *Vs* = 0 V. **c**) Results of KPFS applied between images **a** and **b**. The feedback loop was switched off during the measurements and the sample bias was ramped from zero to a certain negative voltage, then ramped back to zero. The blue and red lines, respectively, show the forward and backward KPFS spectra. The gray arrows indicate the direction of the voltage sweep. The graph to the right of **c** shows the zoomed-out KPFS spectra, indicated by the dashed boxes placed around the regions of frequency jumps between –1.0 and –2.0 V. The tip position is indicated by a blue circle inside the image **a**. **d, e**, Line profiles taken above the oxygen species in panels **a, b** highlighted by different colors.

than that of removing electron O_2^{2-}(B) → O_2^{-}(B). The effect of the negative bias here is to lift up the molecule and thereby facilitate its motion from the B toward the I site without redox state manipulation. Note that, applying positive bias to O_2^{2-}(B) results in creation of an $O_{ad}^{2-} - O_{ad}^{2-}$ adatom pair, see Figure S3. This finding is also in line with DFT simulations suggesting a very minor, 0.07 eV, energy difference between O_2^{2-}(B) and O_2^{2-}(I), see Figure 2. Simulations also predict an inability to induce any rotation onto the O_2^{2-}(B) molecule which prefers to make a O_2^{2-}(B) → O_2^{2-}(I) jump rather than to sustain the huge energy penalty associated with the attempted rotation, see Figure S13. Further KPFS manipulation of O_2^{2-}(I) results in $O_{ad}^{2-} - O_{ad}^{2-}$, a closed shell oxygen adatom species, as shown in the Figure S2. The O_2^{2-}(I) → $O_{ad}^{2-} - O_{ad}^{2-}$ reaction agrees well with our previous results.[15]

2.3. Tip-Induced Peroxo Molecule Rotation

Given the inclination of the O_2^{2-}(I) peroxo molecule with respect to the oxygen rows, one may wonder if the inclination of the molecule can be tip modified. As demonstrated in Figure 4a-c, this is indeed possible. Motivated by the possibility of inducing rotation between the two bistable orientations of O_2^{2-}(I), L and R, see Figure 4, we measured the rates of the rotational process. We moved the tip off the molecular axis to the position indicated by the green circle in Figure 4a, and applied bias voltage to induce the rotation. The Δf signal was measured by changing the bias voltage, Figure 4d, and tip height, Figure 4e, to quantify the rotational rate[43–45] by measuring the telegraph noise. Figure 4f,g shows the rotational rates as a function of applied bias and tip height, respectively. From Figure 4f,g we found that both the L→R and R→L rotational rates increase with negative bias and decrease with tip height. Note that tunneling currents do not flow during this manipulation due to the sizeable band gap of TiO_2, Figure S4.

To clarify the rotational mechanism, we brought the tip far away from the target O_2^{2-}(I) molecule, and applied a large negative bias to the sample. Figure 4b shows an AFM image of O_2^{2-}(I) in orientation R. After obtaining the AFM image, the feedback loop was switched off and the tip was moved 1.3 nm laterally and 1.0 nm vertically away from the O_2^{2-}(I) and the bias was then ramped from zero to –7.0 V and then back to zero, Figure 4h. Figure 4c shows the AFM image of the same scan area obtained at 0 V immediately after ramping the voltage, which shows that the molecular orientation changed from R to L, see Figure S5 for more data. This experimental result demonstrates that the molecule rotated under the large applied negative bias of –7.0 V even though the tip was positioned far away from the target O_2^{2-}(I) molecule indicating that the manipulation mechanism is activated by local electric field.

When a negative bias is applied to O_2^{2-}(I) (the tip has a relative positive charge) the attractive force between the negatively charged O_2^{2-}(I) and the positively charged tip apex results in a slight lifting up of the molecule and the effective bond between the molecule and the surface is reduced. As a result, the potential barrier between the L and R orientations decreases, causing

© 2025 The Author(s). ChemCatChem published by Wiley-VCH GmbH

18673899, 0, Downloaded from https://chemistry-europe.onlinelibrary.wiley.com/doi/10.1002/cctc.202501138 by The University Of Osaka, Wiley Online Library on [11/12/2025]. See the Terms and Conditions (https://onlinelibrary.wiley.com/terms-and-conditions) on Wiley Online Library for rules of use; OA articles are governed by the applicable Creative Commons License

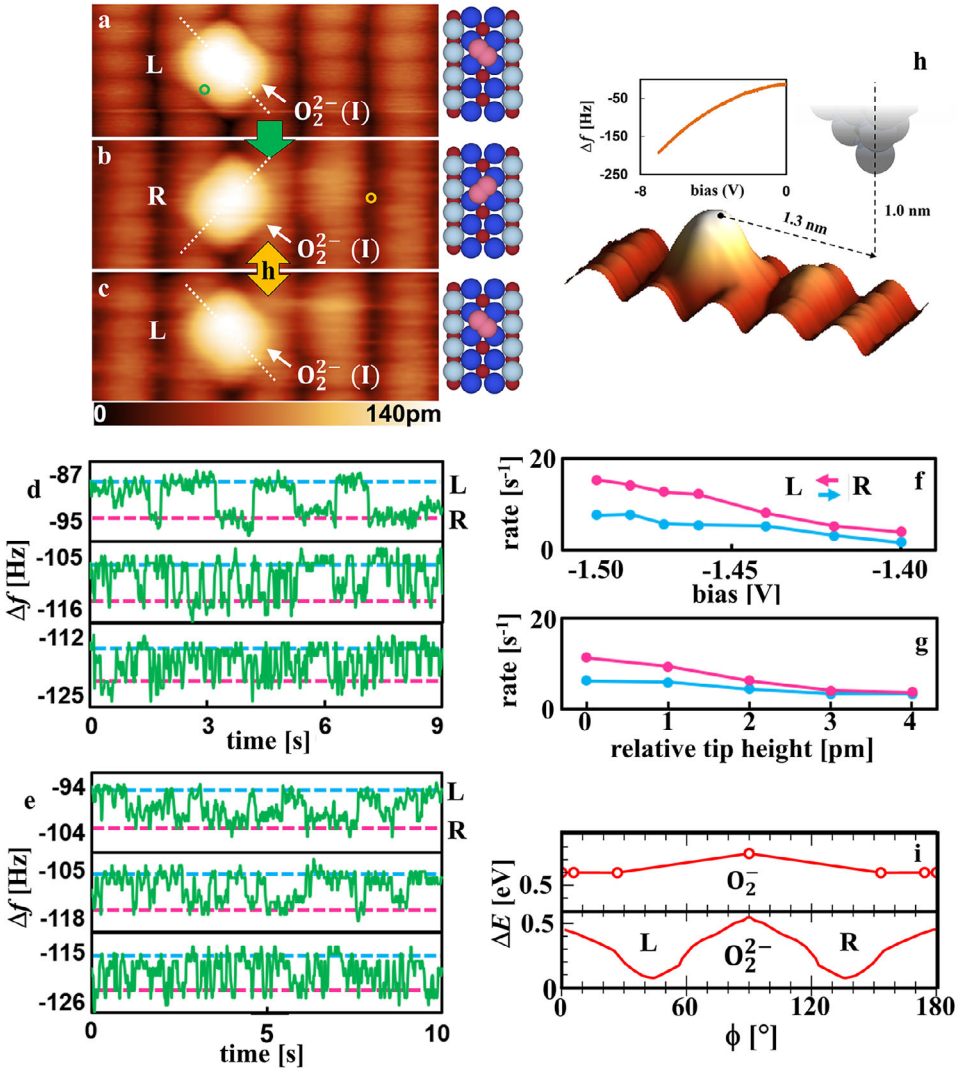

Figure 4. Tip-induced molecular rotation of peroxo molecule. a) AFM image of O_2^{2-}(I) adsorbed on rutile TiO_2(110) surface: orientation L. **b**) AFM image of O_2^{2-}(I) taken after measuring the telegraph noise with the tip position indicated by a green circle. **c**) AFM image after applying electric field far away from the peroxo O_2^{2-}(I) molecule; tip position indicated by an orange circle. Ball and stick models of the on-surface O_2^{2-}(I) peroxo molecule are depicted on the right of images **a–c**. Imaging parameters: constant Δ^f mode, V_s = 0 V. **d**), **e**), Example of time evolution of Δf taken at, from top to bottom, –1.41, –1.47, and –1.50 V voltages and tip heights, from top to bottom of 4, 2, and 0 pm at V= –1.41 V. **f**), **g**) Rotational rates obtained at several sample biases and tip heights. The pink dots correspond to R→L process, the light blue dots to L→R. **h**) Schematic of molecular rotation activated at a large tip-sample distance (1.3 nm laterally and 1.0 nm vertically measured from O_2^{2-}(I)) with the feedback loop was switched off. The inset shows the corresponding KPFS spectroscopy. **i**) DFT computed rotational barriers for O_2^{2-} (I) and O_2^- (I).

the molecule to rotate. This proposed electric mechanism is also supported by applying electric field in the opposite direction (for experimental results with positive sample bias, see Figure S5). As expected, the molecule does not rotate under positive bias. This is in stark contrast with the result of Ref. [31]. where O_2^{2-}(I) rotation and an apparent sideways jump was observed in positive bias. Figure 4f,g show that the R→L rotation rate is always higher than the L→R under the negative bias. Such a spatial rate dependence can be explained by the fact that the electric field is larger when the molecule is close to the tip apex (orientation R), while the electric field is smaller when the molecule is further away from the tip apex (orientation L).

The DFT simulations, Figure 4i, suggest sizeable rotational barriers for on-top peroxo and negligible for on-top superoxo molecules. The peroxo molecule rotational behavior is consistent with the DFT result which suggests a rotational barrier of ≈ 0.4 eV. This value represents an upper limit, as no electric field was considered in the calculation. As discussed above, application of negative bias will lift up the molecule and presumably reduce the rotational barrier height. Rotational activation of the superoxo molecule was not achieved experimentally. DFT simulation suggests a very minute rotational barrier of ≈0.15 eV meaning that the superoxo molecule would be rotationally fairly mobile even at low temperatures.

Given the calculated DFT barrier of ≈0.4 eV and the experimental temperature of 78 K, it would be interesting to determine if the activation source is primarily the electric field or temperature. This could be clarified by quantitatively comparing the rotation rates obtained from temperature-dependent experiments (Arrhenius plot analysis) using energy barriers calculated by DFT

© 2025 The Author(s). ChemCatChem published by Wiley-VCH GmbH

18673899, 0, Downloaded from https://chemistry-europe.onlinelibrary.wiley.com/doi/10.1002/cctc.202501138 by The University Of Osaka, Wiley Online Library on [11/12/2025]. See the Terms and Conditions (https://onlinelibrary.wiley.com/terms-and-conditions) on Wiley Online Library for rules of use; OA articles are governed by the applicable Creative Commons License

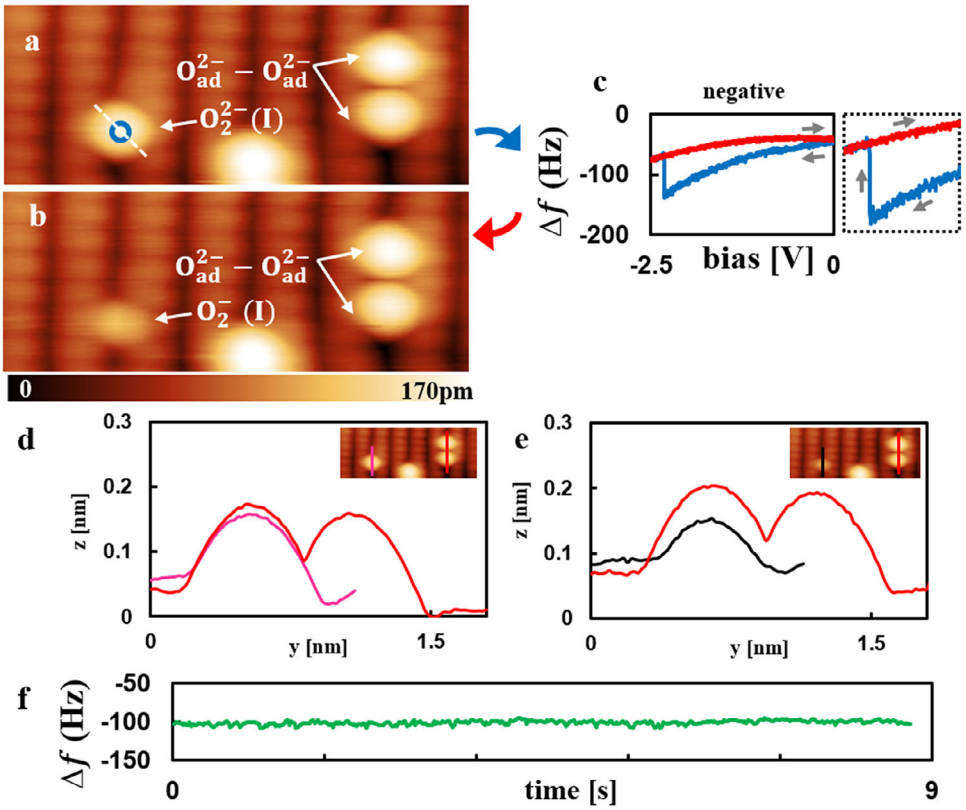

Figure 5. Open shell oxygen molecule synthesis. a) AFM image of O_2^{2-}(I) adsorbed on the rutile TiO_2(110) surface. **b**) AFM image after KPFS manipulation of O_2^{2-}(I) with the tip positioned on top of the target oxygen species. Imaging parameters for **a, b**; constant Δ^f mode, *Vs* = 0 V. **c**) Results of KPFS applied between images **b** and **c**. The feedback loop was switched off during the measurements and the sample bias was ramped from zero to a certain negative voltage, then ramped back to zero. The blue and red lines, respectively, show the forward and backward KPFS spectra. The tip position is indicated by a blue circle inside the images **a**. The gray arrows indicate the direction of the voltage sweep. The graph to the right of panel **c** shows the zoomed-out KPFS spectra indicated by the dashed boxes placed around the regions of frequency jumps between –1.7 and –2.5 V. **d), e**) Line profiles taken above the oxygen species in a, b highlighted by different colors. **f**) $\Delta f(t)$ measurement obtained on top of O_2^-(I) using constant height mode at 0 V. The Δf signal was measured on top of the O_2^-(I) until the tip reached an unreliable drift condition.

under applied electric field. Although no variable-temperature experiments have been performed in the present study, it could provide valuable insights in future experiments.[45] The electric field strength depends not only on the tip–sample distance and applied voltage, but also on microscopic details of the AFM tip. Therefore, quantitatively the rotation rates plotted in Figure 4f,g are expected to depend also on the precise tip shape. Nevertheless, we believe that the qualitative trends of the rates with respect to tip–sample distance and applied voltage are robust and independent of the tip shape details.

2.4. Preparing Superoxo Molecule by Hole Injection

The observed molecular oxygen species in Figures 1, 3, and 4 are all closed shell. Next, we show that a singly charged on-surface open shell molecular ROS, can be synthetized on rutile TiO_2 surface by tip-induced hole injection, for full data set, see Figure S6. Figure 5a shows the peroxo molecule O_2^{2-}(I) that adsorbs on top of substrate Ti_{5c} atom. After imaging Figure 5a, the tip was positioned on top the O_2^{2-}(I) and the voltage was ramped from zero in the negative bias until a steep jump in Δf occurred, and then back to zero, Figure 5c. Figure 5b is the AFM image taken at 0 V of the same scan area immediately thereafter, showing that the image of O_2^{2-}(I) changed into a small bright spot associated with O_2^-(I), indicating that formation of a molecule was catalyzed by removal of one electron from the O_2^{2-}(I). For more results of O_2^-(I) synthesis, see Figure S7.

From comparison of Figure 5d,e, it is evident that the topographic height of superoxo O_2^-(I) molecule is lower than that of the peroxo O_2^{2-}(I) molecule. These differences in topographic images are reproduced by DFT simulations in Figure 2. The DFT calculations indicate that the superoxo molecules are energetically significantly less favorable, a finding valid equally for the oxygen adatoms.[15] Our experimental results clearly show that the superoxo O_2^-(I) molecule while not found spontaneously adsorbed on the rutile TiO_2(110) surface, can readily be prepared on the surface by hole injection. To the best of our knowledge, this is the first observation of a tip-synthetized superoxo O_2^-(I) species on rutile TiO_2 surface by redox-state manipulation. In the related Ref. [31,32] the only redox state manipulations reported were either electron-mediated O_2 dissociation, studied also in Ref. [15] and also here in Figures S2 and S3, or a hole-mediated desorption process.

For application in photocatalysis, a long lifetime of O_2^- is crucial as it must remain active on the TiO_2 surface long enough to

© 2025 The Author(s). ChemCatChem published by Wiley-VCH GmbH

18673899, 0, Downloaded from https://chemistry-europe.onlinelibrary.wiley.com/doi/10.1002/cctc.202501138 by The University Of Osaka, Wiley Online Library on [11/12/2025]. See the Terms and Conditions (https://onlinelibrary.wiley.com/terms-and-conditions) on Wiley Online Library for rules of use; OA articles are governed by the applicable Creative Commons License

decompose the organic substances or CO.[1,3] To investigate the lifetime of O_2^-(I), we positioned the AFM tip directly above the O_2^-(I) molecule and recorded Δf(t) with feedback off. As shown in Figure 5f, we found that the lifetime of O_2^-(I) exceeded 8 s. These results suggest that, under UHV and low-temperature conditions, decomposition can proceed as long as the substances to be decomposed by O_2^-(I) are present in its vicinity during its lifetime.

On-surface open-shell species, albeit atomic rather than molecular, O_{ad}^-, can be synthetized by a two-step tip-assisted redox state reaction: O_2^{2-}(I) → $O_{ad}^{2-} - O_{ad}^{2-}$ → $O_{ad}^- - O_{ad}^-$. Such reactions were studied in detail previously[15] and a short account is shown in Figure S8. Hence, open-shell reactive ROS for photocatalytic applications are expected to be designable via electron–hole activation. Here we found O_2^- and O_{ad}^- which are both open-shell and thus highly reactive. Consequently, on-surface O_2^- and O_{ad}^-, designed via tip-assisted redox reactions, are believed to be of critical importance in photocatalytic applications, such as CO oxidation and the decomposition of organic molecules.

2.5. Preparing Ozone Molecule by KPFS Manipulation

Finally, we demonstrate the tip-assisted on-surface ozone molecule formation. Although ozone is an important ROS in photocatalysis on TiO_2 surfaces,[14] to the best of our knowledge, it has not yet been observed at atomic resolution. Based on macroscopic experiments, previous research has suggested that ozone forms from atomic and molecular oxygen.[42]

In this study, we directly activate and associate three atomic oxygens to synthesize ozone on the rutile TiO_2 surface. Figure 6a shows an atomically resolved AFM image of the rutile TiO_2(110)-(1 × 1) surface after exposure to oxygen at room temperature. Two smaller and one large bright spot of oxygen adatoms can be observed on top of the Ti rows, which can be assigned as a singly charged $O_{ad}^- - O_{ad}^-$ adatom pair and a doubly charged O_{ad}^{2-} adatom, forming the atomic precursors. In order to induce the adatom association, we laterally manipulated the O_{ad}^{2-} adatom, Figure 6a. After AFM imaging, Figure 6a, the tip was brought slightly off from the O_{ad}^{2-} site as indicated by the blue circle, and the bias was ramped from zero to negative direction and then back to zero. Figure 6b shows the AFM image of the same scan area immediately afterward obtained at 0 V, clearly showing that an ozone, O_3, molecule was formed, as illustrated by the model in Figure 6c,d. We presume that the manipulation mechanism is a combination of the local electric field effect combined with a redox reaction leading to electron removal. Application of a negative bias induces an attractive force between the positively charged tip and negatively charged O_{ad}^{2-} adatom causing its motion toward the tip, akin to Langmuir-Hinshelwood reaction. Figure 6e indicates the bias at which the reaction starts. Simultaneously, electrons are removed from the negatively charged adatoms forming the ozone molecule to the tip, resulting in stabilization of the on-surface O_3 molecule. The lateral manipulation of oxygen species preceding its formation is reproducible, and a detailed statistical analysis of these manipulations has been reported in Ref. [17]. In the present study, we emphasize that the critical finding is the direct involvement of the migrated oxygen atom in formation of O_3, which provides the key insight into the underlying reaction pathway.

Although experimentally, we are not able to directly determine the charge state of the ozone molecule formed, DFT simulations strongly suggest that the redox state of the ozone molecule is –2, i.e., corresponds to the O_3^{2-}(A) species in Figure 2. All the other species considered were either sticking out of the surface rather than being adsorbed flat on the surface, were symmetrically adsorbed, or were very high in energy, see Figures S14–S16. Note that we observe only a single Δf jump in Figure 6e. This is because the three-atom association and charge transfer occur simultaneously in time too short to be resolved experimentally. Furthermore, the topographic height of one of the oxygen adatoms in the AFM image the ozone molecule appears higher, yellow arrow in Figure 6b. This observation may be attributed to a distinct charge state or adsorption height relative to the other two atoms. A similar observation was noted with water molecules, where rotation necessitates slight adjustments on NaCl, leading to a small energy barrier.[46] Gas-phase ozone has a 1.5 bond order of the three oxygen adatoms which may be strongly perturbed by the TiO_2 surface and/or polarons localized in the surface. The simulated image in Figure 2 calculated from the local potential without the tip also reveals image contrast between the three ozone atoms, two showing higher and one lower contrast.

As shown in Figure 6f, we measured the lifetime of the on-surface ozone molecule by assessing the $\Delta f(t)$ signal under 0 V bias. The tip was placed on top of the ozone molecule, and the feedback was switched off. Figure 6f suggests a very long lifetime of the ozone molecule exceeding 200 s.

3. Conclusions

Using AFM, KPFS, and DFT simulations, we investigated closed- and open-shell reactive oxygen molecules and adatoms adsorbed on rutile TiO_2(110) surface at 78 K under ultrahigh vacuum. We managed to identify with atomic resolution doubly and singly charged adatoms (O_{ad}^{2-}, O_{ad}^-), adatom pairs ($O_{ad}^{2-} - O_{ad}^{2-}$, $O_{ad}^- - O_{ad}^-$, $O_{ad}^{2-} - O_{ad}^-$) and two adsorption states of the peroxo molecule (O_2^{2-}(I), O_2^{2-}(B)). Oxygen molecules are metastable but can still be observed at low temperatures despite their adsorption energies being up to ≈1.5 eV higher than the ground state $O_{ad}^{2-} - O_{ad}^{2-}$ species.[15] The two peroxide adsorption states are only marginally, ≈0.07 eV, separated in energy and can be manipulated by the AFM tip. We managed to manipulate the rotational state of the O_2^{2-}(I) molecule and we have determined R↔L rotational rates as a function of applied bias and tip-molecule distance. The superoxo O_2^- molecule is always significantly less stable than the peroxide molecule, by ≈0.6 in the O_2^-(I) state and ≈0.85 in the O_2^-(B) state, but it exhibits long life time on rutile TiO_2 surface. The superoxo O_2^-(I) molecule could be prepared by a hole injection to the O_2^{2-}(I) peroxide molecule.

© 2025 The Author(s). ChemCatChem published by Wiley-VCH GmbH

18673899, 0, Downloaded from https://chemistry-europe.onlinelibrary.wiley.com/doi/10.1002/cctc.202501138 by The University Of Osaka, Wiley Online Library on [11/12/2025]. See the Terms and Conditions (https://onlinelibrary.wiley.com/terms-and-conditions) on Wiley Online Library for rules of use; OA articles are governed by the applicable Creative Commons License

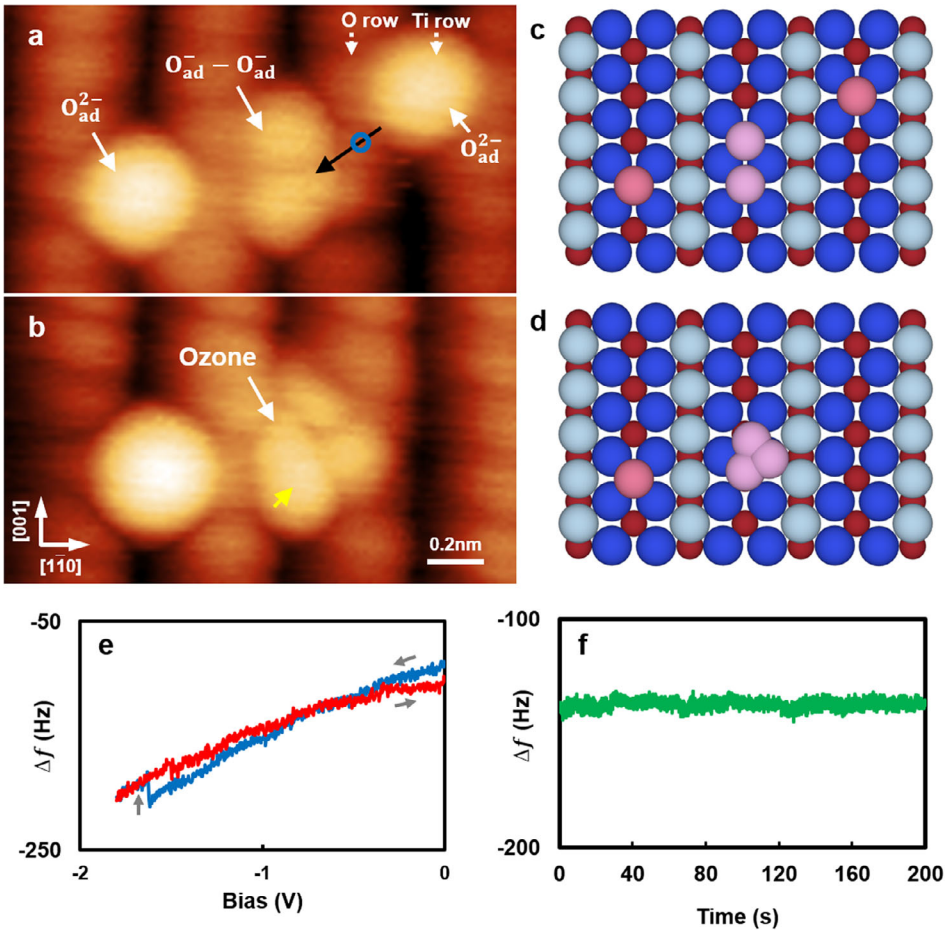

Figure 6. Ozone molecule synthesis on rutile TiO_2 (110) surface via tip-induced Langmuir–Hinshelwood reaction. a), b) Sequential AFM images before and after applying the KPFS in the vicinity of the precursor adatoms. Imaging parameters: constant Δf mode, $V_{bias} = 0$ V. The yellow arrow in **b** indicates an oxygen adatom with a higher topographic height compared to the others. **c), d)** Ball model of the upper layer of the rutile TiO_2(110)-(1 × 1) surface and the oxygen species. **e**) Application of KPFS between **a** and **b** with the tip position indicated by a blue circle in **a**. **f**) The time resolved Δf signal measured on top of the ozone molecule. The Δf signal was measured on top of the ozone molecule with the feedback turned off until the tip reached an unstable drift condition.

Finally, for the first time, we managed to synthetize and visualize the on-surface ozone molecule synthesis with atomic resolution. All this proves the high degree of atomic-scale control we have over all the adsorbed oxygen species and shows a novel route for characterizing and manipulating the oxygen molecules on atomic scale and opens a door for further investigation of suitable molecular and atomic photocatalytic agents on the TiO_2 surface on other insulating and metal oxide surfaces such as, Fe_3O_4, CuO, or CeO_2.

3.1. Experimental Methods and Simulations

The experiments were carried out using low-temperature UHV AFM system. Deflection of the cantilever was measured using optical beam deflection method. The base pressure was lower than 5.0×10^{-11} Torr. The temperature of the AFM unit was kept at liquid nitrogen temperature (78 K). The AFM/KPFS measurements were performed in the frequency modulation detection mode. The cantilever was oscillated at resonance frequency keeping the oscillation amplitude constant. We used iridium (Ir)-coated Si cantilever (Nano sensors SD-T10L100, $f_0 = 800$ kHz, $A = 500$ pm). Metal Ir tips provide stable AFM imaging compared to the bare Si tips. The tip was initially annealed to 600 K and then cleaned by Ar^+ sputtering to remove the contamination before experiments. The rutile TiO_2 (110) – (1 × 1) sample was prepared by sputtering and annealing to 900 K in several cycles. The sample was exposed to oxygen at room temperature for ~ 0.5 L and then transferred to the measurement chamber precooled to 78 K. The atom tracking method was used to compensate the thermal drift between the tip and surface during the specific measurements. The AFM imaging was performed using constant Δ^f mode at $V_s = 0$ V to avoid the tunneling current to flow. The oxygen adatom/molecule charge state manipulation was performed by repeating the cycle of AFM scanning ↔ KPFS (turning off the feedback and ramping the bias from 0 V in the negative or positive direction then ramping back the voltage to 0 V) above the target species. The relative negative/positive bias voltage tended to induce electron removal/attachment and induce structure reconfiguration by the attractive/repulsive interaction by the electric field between tip and sample. The bias voltage of the Δf jump strongly depends on the voltage ramping

© 2025 The Author(s). ChemCatChem published by Wiley-VCH GmbH

18673899, 0, Downloaded from https://chemistry-europe.onlinelibrary.wiley.com/doi/10.1002/cctc.202501138 by The University Of Osaka, Wiley Online Library on [11/12/2025]. See the Terms and Conditions (https://onlinelibrary.wiley.com/terms-and-conditions) on Wiley Online Library for rules of use; OA articles are governed by the applicable Creative Commons License

speed and lateral tip position,[29,36,37] and it indicates qualitatively the success of the charge manipulation and structure reconfiguration.

Customary pseudopotential DFT modeling techniques with hybrid PBE0[47] functional have been used to support the experiments. Detailed description of DFT simulations is in Supporting Information.

Supporting Information

The Supporting Information is available free of charge on the Publications website at DOI: It consists of additional methods and data figures (PDF).

Acknowledgments

This work was supported by a Grant-in-Aid for Scientific Research from Japan Society for the Promotion of Science (JSPS) from the Ministry of Education, Culture, Sports, Science, and Technology of Japan (16H06327, 17H010610, 21J103560, and 22H00282). This work was also supported by the International Joint Research Promotion Program of Osaka University (J171013014, J171013007, J181013004, J181013006, JA1999001, JA19990011, and A21J103560) and JSPS-the National Natural Science Foundation of China (J191053055). This work was also supported by APVV-21–0272, VEGA 2/0133/25, and 2/0131/23 projects and co-funded by the EU NextGenerationEU through the Recovery and Resilience Plan for Slovakia under the project Nos. 09I02-03-V01-00012 and 09I05-03-V02-00055. The DFT calculations were done on the Devana supercomputer under the projects p488-24-1 and p453-24-t.

Conflict of Interests

The authors declare no conflict of interest.

Data Availability Statement

The data that support the findings of this study are available from the corresponding author upon reasonable request.

Keywords: Atomic force microscopy · Charge manipulation · Reactive oxygen molecule · TiO_2

[1] Y. Yoon, Y.-G. Wang, R. Rousseau, V.-A. Glezakou, *ACS Catal.* **2015**, *5*, 1764–1771, https://doi.org/10.1021/cs501873m.
[2] J. Lee, D. C. Sorescu, X. Deng, *J. Am. Chem. Soc.* **2011**, *133*, 10066–10069, https://doi.org/10.1021/ja204077e.
[3] Z. Zhang, J. T. Yates, *J. Am. Chem. Soc.* **2010**, *132*, 12804–12807, https://doi.org/10.1021/ja106207w.
[4] S. Tan, H. Feng, Y. Ji, Y. Wang, J. Zhao, A. Zhao, B. Wang, Y. Luo, J. Yang, J. Hou, *J. Am. Chem. Soc.* **2012**, *134*, 9978–9985, https://doi.org/10.1021/ja211919k.
[5] H. H. Chen, C. E. Nanayakkara, V. H. Grassian, *Chem. Rev.* **2012**, *112*, 5919–5948, https://doi.org/10.1021/cr3002092.
[6] Y. Kakuma, A. Y. Nosaka, Y. Nosaka, *Phys. Chem. Chem. Phys.* **2015**, *17*, 18691–18698, https://doi.org/10.1039/C5CP02004B.
[7] Y. Nosaka, A. Y. Nosaka, *Chem. Rev.* **2017**, *117*, 11302–11336, https://doi.org/10.1021/acs.chemrev.7b00161.
[8] T. Hirakawa, Y. Nosaka, *Langmuir* **2002**, *18*, 3247–3254, https://doi.org/10.1021/la015685a.
[9] S. Wendt, P. T. Sprunger, E. Lira, G. K. Madsen, Z. Li, J. Ø. Hansen, J. Matthiesen, A. Blekinge-Rasmussen, E. Lægsgaard, B. Hammer, F. Besenbacher, *Science* **2008**, *320*, 1755–1759, https://doi.org/10.1126/science.1159846.
[10] M. Setvin, C. Franchini, X. Hao, M. Schmid, A. Janotti, M. Kaltak, C. Walle, G. Kresse, U. Diebold, *Phys. Rev. Lett.* **2014**, *113*, 086402, https://doi.org/10.1103/PhysRevLett.113.086402.
[11] C. M. Yim, M. B. Watkins, M. J. Wolf, C. L. Pang, K. Hermansson, G. Thornton, *Phys. Rev. Lett.* **2016**, *117*, 116402, https://doi.org/10.1103/PhysRevLett.117.116402.
[12] H. Onishi, Y. Iwasawa, *Surf. Sci.* **1994**, *313*, L783–L789, https://doi.org/10.1016/0039-6028(94)91146-0.
[13] M. Reticcioli, M. Setvin, X. Hao, P. Flauger, G. Kresse, M. Schmid, U. Diebold, C. Franchini, *Phys. Rev. X* **2017**, *7*, 031053.
[14] U. Diebold, *Surf. Sci. Rep.* **2003**, *48*, 53–229, https://doi.org/10.1016/S0167-5729(02)00100-0.
[15] Y. Adachi, H. F. Wen, Q. Z. Zhang, M. Miyazaki, Y. Sugawara, H. Q. Sang, J. Brndiar, L. Kantorovich, I. Štich, Y. J. Li, *ACS Nano* **2019**, *13*, 6917–6924, https://doi.org/10.1021/acsnano.9b01792.
[16] Q. Z. Zhang, Y. J. Li, H. F. Wen, Y. Adachi, M. Miyazaki, Y. Sugawara, R. Xu, Z. H. Cheng, J. Brndiar, L. Kantorovich, *J. Am. Chem. Soc.* **2018**, *140*, 15668–15674, https://doi.org/10.1021/jacs.8b07745.
[17] Q. Zhang, H. F. Wen, Y. Adachi, M. Miyazaki, Y. Sugawara, R. Xu, Z. H. Cheng, Y. J. Li, *J. Phys. Chem. C* **2019**, *123*, 28852–28858, https://doi.org/10.1021/acs.jpcc.9b10304.
[18] Y. Du, Z. Dohnalek, I. Lyubinetsky, *J. Phys. Chem. C* **2008**, *112*, 2649–2653, https://doi.org/10.1021/jp077677u.
[19] Z. T. Wang, N. A. Deskins, I. Lyubinetsky, *J. Phys. Chem. Lett.* **2012**, *3*, 102–106, https://doi.org/10.1021/jz2014055.
[20] Y. Du, N. A. Deskins, Z. Zhang, Z. Dohnalek, M. Dupuis, I. Lyubinetsky, *Phys. Chem. Chem. Phys.* **2010**, *12*, 6337, https://doi.org/10.1039/c000250j.
[21] E. Lira, J. Ø. Hansen, P. Huo, R. Bechstein, P. Galliker, E. Lægsgaard, B. Hammer, S. Wendt, F. Besenbacher, *Surf. Sci.* **2010**, *604*, 1945–1960, https://doi.org/10.1016/j.susc.2010.08.004.
[22] J. Matthiesen, S. Wendt, J. Ø. Hansen, G. K. Madsen, E. Lira, P. Galliker, E. K. Vestergaard, R. Schaub, E. Lægsgaard, B. Hammer, F. Besenbacher, *ACS Nano* **2009**, *3*, 517–526, https://doi.org/10.1021/nn8008245.
[23] J. Ø. Hansen, J. Matthiesen, E. Lira, L. Lammich, S. Wendt, *Surf. Sci.* **2017**, *666*, 113–122, https://doi.org/10.1016/j.susc.2017.09.001.
[24] Y. Du, N. A. Deskins, Z. Zhang, Z. Dohnálek, M. Dupuis, I. Lyubinetsky, *J. Phys. Chem. C* **2009**, *113*, 666–671, https://doi.org/10.1021/jp807030n.
[25] Y. Du, N. A. Deskins, Z. Zhang, Z. Dohnalek, M. Dupuis, I. Lyubinetsky, *Phys. Rev. Lett.* **2009**, *102*, 096102, https://doi.org/10.1103/PhysRevLett.102.096102.
[26] Z. T. Wang, Y. Du, Z. Dohnálek, I. Lyubinetsky, *J. Phys. Chem. Lett.* **2010**, *1*, 3524–3529, https://doi.org/10.1021/jz101535f.
[27] S. Tan, Y. Ji, Y. Zhao, A. Zhao, B. Wang, J. Yang, J. G. Hou, *J. Am. Chem. Soc.* **2011**, *133*, 2002–2009, https://doi.org/10.1021/ja110375n.
[28] H. F. Wen, H. Sang, Y. Sugawara, Y. J. Li, *Phys. Chem. Chem. Phys.* **2020**, *22*, 19795–19801, https://doi.org/10.1039/D0CP03549A.
[29] Y. Adachi, J. Brndiar, H. F. Wen, Q. Zhang, M. Miyazaki, S. Thakur, Y. Sugawara, H. Sang, Y. J. Li, I. Štich, L. Kantorovich, *Commun. Mater.* **2021**, *2*, 71.
[30] Y. Adachi, H. F. Wen, Q. Zhang, M. Miyazaki, Y. Sugawara, J. Brndiar, L. Kantorovich, I. Štich, Y. J. Li, *J. Phys. Chem. C* **2022**, *126*, 5064–5069.
[31] I. Sokolovič, M. Reticciolia, M. Čalkovský, M. Wagner, M. Schmid, C. Franchini, U. Diebold, M. Setvín, *Proc. Natl. Acad. Sci. U.S.A.* **2020**, *117*, 14827–14837, https://doi.org/10.1073/pnas.1922452117.
[32] M. Setvin, J. Hulva, G. S. Parkinson, M. Schmid, U. Diebold, *Proc. Natl. Acad. Sci* **2017**, *114*, E2557, https://doi.org/10.1073/pnas.1618723114.
[33] F. J. Giessibl, *Rev. Mod. Phys.* **2003**, *75*, 949–983, https://doi.org/10.1103/RevModPhys.75.949.
[34] L. Gross, F. Mohn, P. Liljeroth, J. Repp, F. J. Giessibl, G. Meyer, *Science* **2009**, *324*, 1428–1431, https://doi.org/10.1126/science.1172273.

© 2025 The Author(s). ChemCatChem published by Wiley-VCH GmbH

18673899, 0, Downloaded from https://chemistry-europe.onlinelibrary.wiley.com/doi/10.1002/cctc.202501138 by The University Of Osaka, Wiley Online Library on [11/12/2025]. See the Terms and Conditions (https://onlinelibrary.wiley.com/terms-and-conditions) on Wiley Online Library for rules of use; OA articles are governed by the applicable Creative Commons License

[35] S. Fatayer, F. Albrecht, Y. Zhang, D. Urbonas, D. Peña, N. Moll, L. Gross, *Science* **2019**, *325*, 1110–1114.
[36] W. Steurer, S. Fatayer, L. Gross, G. Meyer, *Nat. Commun.* **2015**, *6*, 8353, https://doi.org/10.1038/ncomms9353.
[37] S. Fatayer, B. Schuler, W. Steurer, I. Scivetti, J. Repp, L. Gross, M. Persson, G. Meyer, *Nat. Nanotechnol.* **2018**, *13*, 376–380, https://doi.org/10.1038/s41565-018-0087-1.
[38] B. Zhang, J. K. Johnson, *J. Phys. Chem. C* **2013**, *117*, 17151–17158, https://doi.org/10.1021/jp4059142.
[39] M. Shu, Y. Ying, H. Yang, *Chem. Commun.* **2021**, *57* 1018–1021, https://doi.org/10.1039/D0CC07517E.
[40] K. M. Bulanin, J. C. Lavalley, A. A. Tsyganenko, *J. Phys. Chem.* **1995**, *99*, 10294–10298, https://doi.org/10.1021/j100025a034.
[41] H. Chen, C. O. Stanier, M. A. Young, V. H. Grassian, *The Journal of Physical Chemistry A* **2011**, *115*, 11979–11987, https://doi.org/10.1021/jp208164v.
[42] M. E. Monge, C. George, B. D'Anna, J.-F. Doussin, A. Jammoul, J. Wang, G. Eyglunent, G. Solignac, V. Daële, A. Mellouki, *J. Am. Chem. Soc.* **2010**, *132*, 8234–8235, https://doi.org/10.1021/ja1018755.
[43] B. C. Stipe, M. A. Rezaei, W. Ho, *Science* **1998**, *279*, 1907–1909, https://doi.org/10.1126/science.279.5358.1907.
[44] B. C. Stipe, M. A. Rezaei, W. Ho, *Phys. Rev. Lett.* **1998**, *81*, 1263–1266, https://doi.org/10.1103/PhysRevLett.81.1263.
[45] L. J. Lauhon, W. Ho, *J. Chem. Phys.* **1999**, *111*, 5633–5636, https://doi.org/10.1063/1.479863.
[46] J. Peng, D. Cao, Z. He, J. Guo, P. Hapala, R. Ma, B. Cheng, J. Chen, W. J. Xie, X. Z. Li, *Nature* **2018**, *557*, 701–705.
[47] A. Carlo, V. Barone, *J. Chem. Phys.* **1999**, *110*, 6158–6170.

Manuscript received: July 15, 2025
Revised manuscript received: October 8, 2025
Accepted manuscript online: October 23, 2025
Version of record online: ■■, ■■

© 2025 The Author(s). ChemCatChem published by Wiley-VCH GmbH

18673899, 0, Downloaded from https://chemistry-europe.onlinelibrary.wiley.com/doi/10.1002/cctc.202501138 by The University Of Osaka, Wiley Online Library on [11/12/2025]. See the Terms and Conditions (https://onlinelibrary.wiley.com/terms-and-conditions) on Wiley Online Library for rules of use; OA articles are governed by the applicable Creative Commons License